Submitted to ACS Catal., 4/1/2022, revised 5/3/2022

Mechanism and Dynamics of CO_2 Formation in Formic Acid Decomposition on Pt Surfaces

Rongrong Yin,[1] Bin Jiang,[2,*] and Hua Guo,[1,*]

[1]*Department of Chemistry and Chemical Biology, University of New Mexico, Albuquerque, NM 87131, USA*

[2]*Department of Chemical Physics, School of Chemistry and Materials Science, University of Science and Technology of China, Hefei, Anhui 230026, China*

*: corresponding authors: hguo@unm.edu; bjiangch@ustc.edu.cn

Abstract

The final CO_2 formation step in the decomposition of deuterated formic acid (DCOOH) on Pt surfaces is investigated using density functional theory (DFT) and ab initio molecular dynamics (AIMD) trajectories starting at the relevant transition states. The comparison of our AIMD simulations with the recent experimentally measured translational energy and angular distributions of the desorbed CO_2 led us to the conclusion that the decomposition is dominated by the DCOO* intermediate and the observed thermal and hyperthermal channels of the desorbed CO_2 can be attributed to the reaction at terrace and step sites, respectively. The alternative HOOC* pathway is ruled out based on the poor agreement with the experimental distributions and other evidence. Furthermore, the CO_2 product was found to have significant vibrational excitations, consistent with previous observations of chemiluminescence of CO_2 produced by decomposition of formic acid. These product state distributions are rationalized by the Sudden Vector Projection model.

Keywords: formic acid decomposition, CO_2 hydrogenation, site specificity, post-transition state dynamics, density functional theory, ab initio molecular dynamics

I. Introduction

Intense utilization of fossil fuels in recent decades has led to continuous increases in the CO_2 level in the atmosphere. This greenhouse gas is linked to an array of environmental issues such as global warming and ocean acidification, which have dire ramifications to modern societies. To stop the spiral of destruction, it is imperative to actively reduce CO_2 emission and to develop new and more efficient ways to convert CO_2 to useful chemicals in order to achieve carbon neutrality.[1-2] The catalyzed hydrogenation of CO_2 to formic acid (HCOOH) is one of most effective approaches for carbon recycling,[3] but this is a significant challenge as the stable molecule is very difficult to activate. On the other hand, formic acid is also considered as a promising hydrogen carrier, because of its high H content, liquid form, and low toxicity and flammability. Its decomposition for on-demand H_2 production has been extensively investigated,[4-5] and platinum group elements are thought to be the best catalysts for this process.[6] Indeed, reactive scattering of HCOOH from Pt was found to lead to facile production of CO_2 and H_2.[7-8] Furthermore, the presence of adsorbed atomic oxygen on the surface is known to help the O-H cleavage by forming OH* and eventually H_2O,[9-12] instead of H_2. (Throughout the publication, * is used to denote an adsorbed state.)

In both the hydrogenation of carbon dioxide and decomposition of formic acid on a catalytic metal, there are two possible intermediates, namely formate (HCOO*) and carboxyl (HOOC*). The former is formed by cleaving the O-H bond of formic acid and the latter the H-C bond. So far, experiments have only identified the formation of surface formate.[13] On Pt, for example, adsorbed formate was detected using electron

energy loss spectroscopy (EELS)[9] and Fourier transformed infra-red (FTIR) spectroscopy.[11] DFT calculations on this process suggested that HOOC* formation has a significantly higher barrier than that for HCOO* formation,[14-17] which is consistent with the failure in experimental detection of adsorbed HOOC* species. However, its decomposition to CO_2 has a lower barrier than that from HCOO*.

A detailed characterization of the catalytic mechanism for surface reactions remains challenging because of difficulties in monitoring the kinetic evolution of all intermediate species. Recently, there has been significant progress in experimental determination of surface elementary reaction kinetics by the Göttingen group, using imaging approaches.[18-21] These new experimental techniques are not only capable of measuring kinetic traces of elementary surface reactions, but also provide information on dynamics, such as the translational energy and angular distributions of desorbed products.[22] Such detailed information is vital for theoretical simulations of surface dynamics.[23]

In a recent experiment, Fingerhut et al. investigated the transient thermal decomposition kinetics of deuterated formic acid (DCOOH) on the Pt(111) and Pt(332) surfaces at various O* coverages. These two facets of Pt contain terrace and step sites, which provide information on how defect sites affect the adsorption energy of intermediate species and reaction barriers. There has been ample evidence that catalysis is often dominated by defects, such as steps, vacancies, and kinks.[24-27] Thus, a complete understanding of catalysis cannot be achieved with models based on ideal flat metal surfaces and models with defect sites are needed.

In the experiment, the production of H_2O was found to have a much faster appearance than those of D_2O and CO_2,[28] strongly suggesting that the initial step of O-H bond dissociation is fast, consistent with previous experimental[9] and theoretical studies.[14-17] These observations implied the dominance of the DCOO* intermediate, which can decay subsequently to CO_2 and D*. These authors further reported the angular and translational energy distributions of the final CO_2 product, which forms two distinct channels. The thermal channel features a broad cosine angular distribution, while the hyperthermal channel a sharp angular distribution along the surface normal. However, the origin of these two channels was unknown. In addition, the translational energy distributions of the desorbed CO_2 provided information on the lower limit of reaction barriers leading to the formation of the formate intermediate by hydrogenation of CO_2, providing a test for theory. It is clear that the interpretation of these interesting experimental observations could greatly benefit from theoretical studies of the energetics and dynamics, which have recently undergone significant advances.[23, 29-31] In this work, we report theoretical calculations aimed at a mechanistic interpretation of these detailed experimental observations, which has important implications on the heterogeneous catalyzed CO_2 hydrogenation and HCOOH decomposition.

II. Methods

All periodic density functional theory (DFT) calculations were performed with the Vienna Ab initio Simulation Package (VASP).[32-33] The Bayesian Error Estimation Functional method with van der Waals corrections (BEEF-vdW)[34] was employed. The electron-ion interactions were described by projector augmented wave (PAW)

method.[35] All calculations were performed without spin polarization. The wave function of the valence electrons was expanded using plane waves with an energy cutoff of 400 eV. Fermi smearing with a width parameter of 0.1 eV was used. The flat Pt(111) surface was modeled by a 4-atomic-layer slab, which has a (3 × 3) unit cell with the top three layers relaxed, separated by a 20 Å vacuum space to avoid the interslab interaction. For the stepped Pt(332) surface, a 20-atomic-layer slab was used with a (3 × 1) unit cell was used with the 17 top atomic layers allowed to be relaxed and a 20 Å vacuum space to separate the slabs. The Brillouin zone integration was performed on a 4 × 4 × 1 Gamma *k*-points grid and a 3 × 2 × 1 Monkhorst-Pack *k*-points[36] for the Pt(111) and Pt(332) surfaces, respectively. The convergence criterion was set as 10^{-6} eV for the electronic self-consistency iteration and 0.02 eV/Å for the ionic relaxation in geometric optimization. The geometry was optimized using a conjugate-gradient method. The saddle points were determined using the climbing image nudged elastic band (CI-NEB)[37] and the dimer methods,[38] and confirmed by frequency calculations. The calculated lattice constant for bulk Pt is 3.986 Å, in good agreement with the experimental value of 3.912 Å.[39]

The binding energy (BE) is reported with respect to the desorbed CO_2:

$$BE_{\mathrm{x}} = E_{\mathrm{x@slab}} - E_{\mathrm{H^*@slab}} - E_{\mathrm{CO_2}}$$

where $E_{\mathrm{x@slab}}$ and $E_{\mathrm{H^*@slab}}$ are the total energies of the adsorbate + slab and H* + slab systems and $E_{\mathrm{CO_2}}$ is the energy of the gas-phase CO_2.

Ab Initio Molecular Dynamics (AIMD) simulations were performed with the same DFT protocol. Following our recent work,[40] the post-transition state dynamics were

described by trajectories starting from the transition state geometries. All movable atoms were assigned with random initial velocities according to a Maxwell-Boltzmann distribution at the experimental temperature of 623 K.[28] The dynamics was assumed to be in a micro-canonical NVE ensemble, with constant number (N), volume (V), and energy (E). Approximately 100 trajectories were propagated for each transition state using the leap-frog algorithm implemented in VASP. The time step was set to 1.0 fs and the trajectories were propagated until the CO_2 center of mass reaches 7.0 Å above the surface with the velocity pointing away from the surface.

The center-of-mass translational energy and angular distributions of the desorbed CO_2 were determined along with the internal energy. Specifically, the translational energy (E_t) of the CO_2 molecule was calculated as: $E_t = \frac{1}{2} m_{CO_2} v_{COM}^2$, where the m_{CO_2} is the CO_2 mass and the v_{COM} is its center-of-mass velocity. The vibrational energy (E_v) of the CO_2 molecule was determined as the difference between its internal energy (E_{int}) and rotational energy (E_{rot}), $E_v = E_{int} - E_{rot}$. The rotational energy is given by $E_{rot} = \frac{1}{2} \vec{w} \cdot \vec{j}$, where the $\vec{w}$ is the angular velocity of CO_2, the $\vec{j}$ is the rotational angular momentum of CO_2. The internal energy consists of the kinetic and potential energies of CO_2: $E_{int} = T + V$.

III. Results

Previous DFT calculations have revealed that formic acid (HCOOH) decomposition on Pt surfaces has two possible pathways,[16-17] namely the HCOO* pathway and HOOC* pathway, both eventually leading to the production of H* and desorbed CO_2. The adsorbed H* can subsequently recombine with another H* to form

H_2 or with O* leading to the desorption of H_2O. As discussed in Introduction, overwhelming experimental evidence suggested that the formic acid decomposition is dominated by the initial O-H bond cleavage, leading to the formate intermediate HCOO*.[9-12] The most stable form of HCOO* is believed to be a bidentate species, bi-HCOO*, with both oxygens bonded to the Pt surface.[12] However, this bidentate species cannot directly decompose to CO_2 and it needs to first transform to a monodentate formate species, mono-HCOO*, with one single oxygen bonding to the Pt surface.[41]

To understand the recent experiment of Fingerhut et al.,[28] we consider here the decomposition of DCOOH on two Pt surfaces at zero O* coverage, for which the two aforementioned pathways can be readily identified by the DCOO* and HOOC* intermediates, respectively. We first determined the stationary points along the DCOO* pathway and the results are shown in the upper panel of Figure 1. The DCOO* pathway is denoted as the TR1 (terrace reaction 1) and SR1 (step reaction 1) on the Pt(111) and Pt(332) surfaces, respectively. (Note that deuteration does not change the potential energy.) At the terrace site on Pt(111), bi-DCOO* binds on two nearest neighbor Pt atoms through the two oxygens. Similarly, at the step site on Pt(332), bi-DCOO* also binds on two upper step edge Pt atoms along the Pt-edge through two oxygens, in a top-top configuration. At the transition state (TS1), the bidentate formate pivots gradually towards the monodentate configuration, which has a higher energy with the molecule binds through one O atom and the C-H bond pointing toward the surface. The rotation from bi- to mono-dentate formate has a barrier (TS1) of 1.10 and 1.06 eV for Pt(111) and Pt(332), respectively. The calculated barrier on Pt(111) is in good agreement with

the previous DFT values (1.05[17] and 1.00 eV[16]) with the PW91 functional.

The calculated BE of the bi-DCOO* is 0.31 and -0.36 eV on the terrace and step sites, respectively. These values are in good agreement to those derived from experiment, 0.23 ± 0.08 eV and -0.55 ± 0.07 eV.[28] The calculated relative stability of the intermediate at the two sites is 0.67 eV, which can be compared with the previous theoretical value of 0.66 eV[42] and the experimental estimate of 0.78 ± 0.11 eV.[28]

To understand the decomposition dynamics of mono-DCOO* to CO_2, we performed AIMD simulations with trajectories starting at TS2. Since D is pointed towards the surface at the initial configuration, the incipient CO_2 formed by cleaving the D-C bond experiences a repulsive force that pushes it away from the surface. Figure 2(a) shows the center-of-mass translational energy distribution of the CO_2 product formed in the DCOO* pathway on the Pt(111) and Pt(332) surfaces, denoted in the figure as TR1 and SR1, respectively. It is clear from the figure that CO_2 desorbed from the terrace and step sites has drastically different translational energy distributions: the CO_2 product in the TR1 channel move much faster than that in the SR1 channel. This is partly due to the fact that the TS2 energy relative to the gas phase CO_2 (defined as the energy zero) at the terrace site is much higher than that at the step site. The experimentally observed thermal and hyperthermal channels[28] are indicated in the same figure as dotted lines, which are qualitatively reproduced by our simulations. In particular, the average translation energy is 0.17 and 0.29 eV for the thermal and hyperthermal channels, which can be compared with the experimental values of 0.10 and 0.23 eV.[28] In the experiment,[28] the thermal component is associated with a broad

angular distribution close to cos(θ), where θ is the polar angle from the surface normal, while the hyperthermal channel has a sharp angular distribution close to a $\cos^5(\theta)$ function. The calculated angular distributions from the two Pt surface sites are given Figure 2(b), which show a narrow distribution close to $\cos^5(\theta)$ for CO_2 from the terrace site and a broad distribution close to cos(θ) for CO_2 from the step site.

To shed light on the correlation between the translational energy and angular distributions of the desorbed CO_2, we plot the corresponding distributions of the AIMD trajectories in Figure 3. It is shown that most of CO_2 products from the terrace site have high kinetic energies and desorb near the surface normal. On the other hand, the desorbed CO_2 molecules from the step site have relatively low kinetic energies and spread to large angles. To better understand the dynamics, the distributions are replotted in Figure 3(b) with the translational energy in the *z* direction along the surface normal. The distribution for CO_2 from the step site shows that the off-normal desorption corresponds relatively small kinetic energies along the surface normal. In other words, these trajectories have a relatively large translational energy component along the surface plane. In Supporting Information (SI), the mean translational energy and components of translational energy along the *x*, *y*, *z* and *xy* directions for desorbed CO_2 molecules formed by two different pathways, via the DCOO* and HOOC* intermediates, are shown in Table S1 and some exemplary trajectories are displayed in Figures S1 and S2, both confirming the above explanation. Some of the trajectories diffuse along the surface for a relatively long time, because of the insufficient translational energy in the *z* direction to overcome the desorption barrier. These

diffusive trajectories contribute to the off-normal desorption of CO_2.

To understand the origin of the differences observed in the CO_2 angular and translational energy distributions from the two Pt surfaces, we relied on the Sudden Vector Projection (SVP) model.[43] The SVP model predicts the disposal of energy in reaction products by projecting product normal mode vectors onto the reaction coordinate at the transition state.[44] In the sudden limit where the reaction time is much shorter than that of energy randomization, a large projection implies that the reaction coordinate is aligned with the product mode and thus a strongly coupling, enabling facile energy flow from the reaction coordinate into that product mode. As shown in the Figure 4, the SVP analysis shows the projection value of the CO_2 translational mode along the surface normal (z), t_z, at TS2 on Pt(332) is small, while the corresponding values along the surface (x and y) are quite large. On Pt(111), on the other hand, t_z has the largest projection for TS2. These results, which are consistent with the calculated CO_2 translational energy and angular distributions discussed above, revealed the origin of the product distributions. This underscores the importance of dynamics, in which the energy is disposed along the reaction coordinate.

The SVP analysis also suggests significant vibrational excitation, particularly in the bending mode, in the desorbed CO_2 from both Pt surfaces. This is easy to understand as the CO_2 moiety has a bent configuration at the transition state, while the free CO_2 is linear. The vibrational energy distributions of the CO_2 product from the two surface sites are displayed in Figure 5, which are consistent with previous experimental observations of chemiluminescence from CO_2 produced from decomposition of

HCOOH on Pt surfaces.[45] The experimental estimate of the energy in the CO_2 internal modes is 0.74 ± 0.07 and 0.60 ± 0.07 eV on Pt(111) and Pt(332), respectively.[28] These numbers compare well with our values of 0.71 and 0.41 eV, respectively.

Despite the lack of experimental evidence for its existence, we have also investigated the HOOC* pathway in DCOOH decomposition, which are denoted as TR2 and SR2 on the Pt(111) and Pt(332) surfaces, respectively. The calculated energetics and geometries of the stationary points are shown in the lower panel of Figure 1. The formation of carboxyl (HOOC*) from formic acid starts with the isomerization from the *cis*-HOOC* configuration to a more stable *trans*-HOOC* configuration via the O-H bond rotation.[17] The re-orientation steps on the Pt(111) and Pt(332) surfaces have an activation barrier of 0.36 and 0.43 eV, respectively. The slightly more stable *trans*-HOOC* species on Pt is bound through a Pt-C bond with its O-H bond towards the surface. The barriers of the reverse CO_2 hydrogenation step to *trans*-HOOC* on Pt(111) and Pt(332) are quite close, 0.78 *vs*. 0.84 eV. The barriers of TS2 on the TR2 are consistent with the previous DFT results of 0.67 eV[16], 0.73 eV,[17] and 0.78 eV,[46] with the PW91 functional.

In the subsequent decomposition, there exists a minimum corresponding to chemisorbed CO_2, which has a bent configuration due to electron transfer to the antibonding orbital of the adsorbed molecule.[47] Such a chemisorbed CO_2, which has been identified in our previous work on CO_2 formation through CO oxidation on Pt surfaces,[40] was attributed to the thermal component observed in the experiment.[18] In our case, the barrier of the bent-to-linear transformation is 0.05 and 0.12 eV on Pt(111)

and Pt(332), respectively. The chemisorbed CO_2 on the two surfaces is metastable, as suggested by the positive BE of 0.45 and 0.16 eV, respectively. However, such a species along TR2 and SR2 could in principle impact the translational energy and angular distributions of the CO_2 product.

AIMD simulations for the CO_2 desorption along the HOOC* pathway were performed on the Pt(111) and Pt(332) surfaces, starting from the TS2 geometries. Since the decomposed H is pointed towards the surface, the incipient CO_2 is initially pushed away towards the vacuum. The lower panels of Figure 2 display the translational energy and angular distributions of the CO_2 product formed on the two surface sites. It can be readily seen that both channels have roughly the same translational energy and angular distributions, which is very different from those from the DCOO* pathway presented in the same figure. Both translational energy distributions are hyperthermal and the angular distributions are narrowly centered at the surface normal, although that for the SR2 channel is somewhat broader.

The correlation between kinetic energies and desorption angles of the desorption trajectories is shown in the lower panels of Figure 3 for the TR2 and SR2 pathways. These distributions are consistent with the translational energy and angular distributions shown in Figure 2. Like in the SR1 dynamics, the desorption of CO_2 at large angles features small translational energy along the surface normal, suggesting significant translational energies along the surface plane. Detailed analysis of the trajectories found no trapping in the CO_2 chemisorption well, although some trajectories spend significant time near the surface as CO_2 diffuses along the surface, as results showed in Figure S2

of SI.

The translational energy and angular distributions of the CO_2 product in the HOOC* pathway can also be rationalized by the SVP model, as shown in Figure 4. From the terrace site, the CO_2 product has a large t_z component, which is consistent with the hyperthermal translational energy distribution and narrow angular distribution. At the step site, on the other hand, there is a significant t_x component, suggesting a large translational energy release parallel to the surface and a broader angular distribution. These predictions are consistent with the calculated distributions shown in Figures 2 and 3.

The SVP projections also suggest significant internal excitation in the desorbed CO_2, as in the DCOO* pathways. The vibrational energy distributions of the CO_2 product in the HOOC* pathway are displayed for both surface sites in Figure 5. Comparing with the DCOO* pathway, the internal excitation for TR2 and SR2 are more moderate with the values of 0.26 and 0.23 eV, respectively. There is some rotational excitation as well.

IV. Discussion

The comparison between the calculated and measured translational energy and angular distributions of the desorbed CO_2 from the decomposition of DCOOH suggests that the experimentally observed thermal and hyperthermal components[28] are due to DCOO* decomposition at the terrace and step sites of the Pt surface, respectively. This conclusion is supported by the reasonably good agreement between the experimental and theoretical distributions, as shown in Figure 2. On the other hand, the results from

the HOOC* decomposition are inconsistent with the experimental observations, given the absence of the thermal channel. The relevance of this pathway is further discounted by the experimentally observed fast H_2O trace, which supports the dominant formation of the DCOO* intermediate.[28]

Despite the large energy release available from the corresponding transition state in the DCOO* decomposition, the desorbed CO_2 in the SR1 pathway has relatively low translational energy. According to the SVP model, this dynamical effect can be attributed to the reaction coordinate at the corresponding TS2 that is strongly coupled with the internal modes of CO_2, which channels a large portion of the energy release to the vibrational modes of the desorbing molecule, but weakly coupled to the translational mode along the surface normal. This situation is very similar to the thermal channel of the CO_2 formed by CO oxidation on Pt(332), as discussed in our previous work.[40] However, the formation of a chemisorbed CO_2 found in the CO oxidation process does not seem to be occurring in the current system.

Another interesting observation in the experiment of Fingerhut et al. is that the kinetic traces for the fast and slow components of the desorbed CO_2 are the same. This is quite different from the previous study of CO_2 formed by CO oxidation on Pt surfaces, where different kinetic traces were observed.[18] Our calculations shown in Figure 1 suggest that the barrier for the conversion of bi-DCOO* to mono-DCOO* is roughly the same at the terrace (1.11 eV) and step (1.06 eV) sites, despite much stronger binding energy of the bi-DCOO* on the step site. This agreement further supports our assignment of the thermal and hyperthermal components.

Although the agreement between the TR1 and SR1 results and experiment is quite satisfactory, our simulations could not be reconciled with two important experimental observations. First, Fingerhut et al. reported at the zero O coverage a much larger thermal component than the hyperthermal counterpart and near identical branching ratios between the two components on both Pt(111) and Pt(332), which have significantly different step densities.[28] However, because the DCOO* species is energetically much more favorable at the step site, it is possible the thermal channel is overwhelmingly large and hence insensitive to the step density. Further investigation is needed to resolve this discrepancy. Secondly, the experimentally measured DCOO* decomposition barrier is 0.62 eV, significantly lower than our DFT value of ~1.1 eV. One possibility that the kinetic trace has contributions from the HCOO* pathway, which has an estimated barrier of ~0.8 eV on Pt(111).

Finally, Fingerhut et al. estimated the barriers for CO_2 hydrogenation to bi-DCOO* on Pt(111) and Pt(332) based on the translational energy distribution of desorbed CO_2.[28] Their values are 0.85 $\pm$ 0.06 eV and 0.65 $\pm$ 0.06 eV, respectively, which can be compared with the theoretical values of 1.42 and 0.70 eV. However, the barriers were estimated in the experimental paper from the cutoff of the translational energy distributions,[28] which did not consider the significant internal energy excitation in the CO_2 product. As a result, these numbers should be considered as the lower limits, which are not inconsistent with our DFT values. In Figure S3, the internal energy distributions of CO_2 are shown for all four pathways. The minimum internal energy for TR1 and SR1 is 0.40 and 0.15 eV, respectively. If these energies are added to the translational energy

distributions, the corresponding barrier heights should be corrected to 1.25 and 0.80 eV, respectively, which are much closer to our theoretical predictions. On the other hand, our calculations indicated that the bi-DCOO* is more stable at the step site than at the terrace site by 0.67 eV, in reasonable agreement with the experimental estimate of ~0.8 eV.[28]

V. Summary

To summarize, we report extensive DFT and AIMD calculations for the final gaseous CO_2 product formation step in the formic acid (DCOOH) decomposition on the Pt(111) and Pt(332) surfaces. The geometry and energy of stationary points along the DCOO* and HOOC* pathways of the reaction are determined by DFT and found to agree with available theoretical results. AIMD trajectories launched from the relevant transition states yielded translational energy and angular distributions of the desorbed CO_2 product, which are compared with the experimental observations. The good agreement with the measured CO_2 translational energy and angular distributions led us to conclude that the experimentally observed thermal and hyperthermal channels are due to the decomposition of the DCOO* intermediate at the terrace and step sites of the Pt surfaces, respectively. In agreement with experiment, the barrier for converting bi-DCOO* to mono-DCOO* is about the same on the two surface sites, leading to similar reaction rates. Furthermore, the CO_2 products are found to be internally excited, consistent with the experimentally observed chemiluminescence. On the other hand, the viability of the HOOC* pathway is ruled out by both energetic and dynamic evidence from experimental and theoretical studies. The detailed information provided

by our theoretical calculations is instrumental in understanding not only the formic acid decomposition mechanism, but also related processes such as the hydrogenation of CO_2.

Admittedly the number of AIMD trajectories reported in this work is relatively small, due to the high computational costs. However, we note that machine learning techniques are available to construct analytic high-dimensional potential energy surfaces that allow more efficient trajectory calculations,[48-49] as demonstrated recently for the CO_2 formation on Pt surfaces via CO oxidation.[50]

Finally, we note that our calculations did not consider the impact of the O* coverage, which has been shown experimentally to significantly impact the kinetics.[28] Because of the existence of multiple adsorption sites and of lateral interactions among adsorbed oxygens, the modeling of adsorbed atomic oxygen on the Pt surface at different coverages is much more challenging and require significantly more demanding calculations, which we defer to a future time.

Acknowledgements: This work was supported by the National Science Foundation (CHE-1951328 to H.G.) and by National Natural Science Foundation of China (22073089 to B.J.), K. C. Wong Education Foundation (GJTD-2020-15 to B.J.). H.G. also thanks the Alexander von Humboldt Foundation for a Humboldt Research Award. The computations were carried out at the Center for Advanced Research Computing (CARC) at UNM. The authors thank Jan Fingerhut, Dima Borodin, Theo Kitsopoulos, and Alec Wodtke for extensive discussions.

Supporting Information. Additional calculation results. This material is available free of charge via the Internet at http://pubs.acs.org.

References

1. Arakawa, H., et al., Catalysis Research of Relevance to Carbon Management: Progress, Challenges, and Opportunities. *Chem. Rev.* **2001**, *101*, 953-996.
2. Haszeldine, R. S., Carbon Capture and Storage: How Green Can Black Be? *Science* **2009**, *325*, 1647-1652.
3. Bulushev, D. A.; Ross, J. R. H., Heterogeneous Catalysts for Hydrogenation of CO_2 and Bicarbonates to Formic Acid and Formates. *Catal. Rev.* **2018**, *60*, 566-593.
4. Johnson, T. C.; Morris, D. J.; Wills, M., Hydrogen Generation from Formic Acid and Alcohols Using Homogeneous Catalysts. *Chem. Soc. Rev.* **2010**, *39*, 81-88.
5. Singh, A. K.; Singh, S.; Kumar, A., Hydrogen Energy Future with Formic Acid: A Renewable Chemical Hydrogen Storage System. *Catal. Sci. Technol.* **2016**, *6*, 12-40.
6. Tang, Y.; Roberts, C. A.; Perkins, R. T.; Wachs, I. E., Revisiting Formic Acid Decomposition on Metallic Powder Catalysts: Exploding the Hcooh Decomposition Volcano Curve. *Surf. Sci.* **2016**, *650*, 103-110.
7. Steinbach, F.; Hausen, V., Catalytic Decomposition of Dcood Studied by Reactive Scattering of a Modulated Dcood Nozzle Beam by a Polycrystalline Platinum Surface in Ultra High Vacuum. *Surf. Sci.* **1977**, *62*, 504-518.
8. Gdowski, G. E.; Fair, J. A.; Madix, R. J., Reactive Scattering of Small Molecules from Platinum Crystal Surfaces: D_2CO, CH_3OH, HCOOH, and the Nonanomalous Kinetics of Hydrogen Atom Recombination. *Surf. Sci.* **1983**, *127*, 541-554.
9. Avery, N. R., Reaction of Hcooh with a Pt(111)-O Surface; Identification of Adsorbed Monodentate Formate. *Appl. Surf. Sci.* **1983**, *14*, 149-156.
10. Columbia, M. R.; Crabtree, A. M.; Thiel, P. A., Chemical Reactions between Atomic Oxygen and Formic Acid on Pt(111). *J. Electroanal. Chem.* **1993**, *351*, 207-226.
11. Solymosi, F.; Koós, Á.; Liliom, N.; Ugrai, I., Production of CO-Free H_2 from Formic Acid. A Comparative Study of the Catalytic Behavior of Pt Metals on a Carbon Support. *J. Catal.* **2011**, *279*, 213-219.
12. Silbaugh, T. L.; Karp, E. M.; Campbell, C. T., Energetics of Formic Acid Conversion to Adsorbed Formates on Pt(111) by Transient Calorimetry. *J. Am. Chem. Soc.* **2014**, *136*, 3964-3971.
13. Columbia, M. R.; Thiel, P. A., The Interaction of Formic Acid with Transition Metal Surfaces, Studied in Ultrahigh Vacuum. *J. Electroanal. Chem.* **1994**, *369*, 1-14.
14. Gao, W.; Keith, J. A.; Anton, J.; Jacob, T., Theoretical Elucidation of the Competitive Electro-Oxidation Mechanisms of Formic Acid on Pt(111). *J. Am. Chem. Soc.* **2010**, *132*, 18377-18385.
15. Herron, J. A.; Scaranto, J.; Ferrin, P.; Li, S.; Mavrikakis, M., Trends in Formic Acid Decomposition on Model Transition Metal Surfaces: A Density Functional Theory Study. *ACS Catal.* **2014**, *4*, 4434-4445.
16. Scaranto, J.; Mavrikakis, M., Hcooh Decomposition on Pt(111): A DFT Study. *Surf. Sci.* **2016**, *648*, 201-211.
17. Bhandari, S.; Rangarajan, S.; Maravelias, C. T.; Dumesic, J. A.; Mavrikakis, M., Reaction Mechanism of Vapor-Phase Formic Acid Decomposition over Platinum Catalysts: Dft, Reaction Kinetics Experiments, and Microkinetic Modeling. *ACS Catal.* **2020**, *10*, 4112-4126.
18. Neugebohren, J., et al., Velocity-Resolved Kinetics of Site-Specific Carbon Monoxide Oxidation on Platinum Surfaces. *Nature* **2018**, *558*, 280-283.

19. Shirhatti, P. R.; Rahinov, I.; Golibrzuch, K.; Werdecker, J.; Geweke, J.; Altschäffel, J.; Kumar, S.; Auerbach, D. J.; Bartels, C.; Wodtke, A. M., Observation of the Adsorption and Desorption of Vibrationally Excited Molecules on a Metal Surface. *Nat. Chem.* **2018**, *10*, 592-598.
20. Borodin, D., et al., Following the Microscopic Pathway to Adsorption through Chemisorption and Physisorption Wells. *Science* **2020**, *369*, 1461.
21. Borodin, D.; Schwarzer, M.; Hahn, H. W.; Fingerhut, J.; Wang, Y.; Auerbach, D. J.; Guo, H.; Schroeder, J.; Kitsopoulos, T. N.; Wodtke, A. M., The Puzzle of Rapid Hydrogen Oxidation on Pt(111). *Mole. Phys.* **2021**, *119*, e1966533.
22. Park, G. B.; Kitsopoulos, T. N.; Borodin, D.; Golibrzuch, K.; Neugebohren, J.; Auerbach, D. J.; Campbell, C. T.; Wodtke, A. M., The Kinetics of Elementary Thermal Reactions in Heterogeneous Catalysis. *Nat. Rev. Chem.* **2019**, *3*, 723-732.
23. Jiang, B.; Guo, H., Dynamics in Reactions on Metal Surfaces: A Theoretical Perspective. *J. Chem. Phys.* **2019**, *150*, 180901.
24. Dahl, S.; Logadottir, A.; Egeberg, R. C.; Larsen, J. H.; Chorkendorff, I.; Tornqvist, E.; Nørskov, J. K., Role of Steps in N_2 Activation on Ru(0001). *Phys. Rev. Lett.* **1999**, *83*, 1814-1817.
25. Behrens, M., et al., The Active Site of Methanol Synthesis over $Cu/ZnO/Al_2O_3$ Industrial Catalysts. *Science* **2012**, *336*, 893-897.
26. van Lent, R.; Auras, S. V.; Cao, K.; Walsh, A. J.; Gleeson, M. A.; Juurlink, L. B. F., Site-Specific Reactivity of Molecules with Surface Defects—the Case of H_2 Dissociation on Pt. *Science* **2019**, *363*, 155-157.
27. Gutiérrez-González, A.; Torio, M. E.; Busnengo, H. F.; Beck, R. D., Site Selective Detection of Methane Dissociation on Stepped Pt Surfaces. *Top. Catal.* **2019**, *62*, 859-873.
28. Fingerhut, J.; Borodin, D.; Schwarzer, M.; Skoulatakis, G.; Auerbach, D. J.; Wodtke, A. M.; Kitsopoulos, T. N., The Barrier for CO_2 Functionalization to Formate on Hydrogenated Pt. *J. Phys. Chem. A* **2021**, *125*, 7396-7405.
29. Guo, H.; Jackson, B., Mode- and Bond-Selective Chemistry on Metal Surfaces: The Dissociative Chemisorption of CHD_3 on Ni(111). *J. Phys. Chem. C* **2015**, *119*, 14769-14779.
30. Alducin, M.; Díez Muiño, R.; Juaristi, J. I., Non-Adiabatic Effects in Elementary Reaction Processes at Metal Surfaces. *Prog. Surf. Sci.* **2017**, *92*, 317-340.
31. Kroes, G.-J., Computational Approaches to Dissociative Chemisorption on Metals: Towards Chemical Accuracy. *Phys. Chem. Chem. Phys.* **2021**, *23*, 8962-9048.
32. Kresse, G.; Furthmuller, J., Efficient Iterative Schemes for Ab Initio Total-Energy Calculations Using Plane Wave Basis Set. *Phys. Rev. B* **1996**, *54*, 11169-11186.
33. Kresse, G.; Furthmuller, J., Efficiency of Ab Initio Total Energy Calculations for Metals and Semiconductors Using Plane Wave Basis Set. *Comp. Mater. Sci.* **1996**, *6*, 15-50.
34. Wellendorff, J.; Lundgaard, K. T.; Møgelhøj, A.; Petzold, V.; Landis, D. D.; Nørskov, J. K.; Bligaard, T.; Jacobsen, K. W., Density Functionals for Surface Science: Exchange-Correlation Model Development with Bayesian Error Estimation. *Phys. Rev. B* **2012**, *85*, 235149.
35. Blöchl, P. E., Projector Augmented-Wave Method. *Phys. Rev. B* **1994**, *50*, 17953-17979.
36. Monkhorst, H. J.; Pack, J. D., Special Points for Brillouin-Zone Integrations. *Phys. Rev. B* **1976**, *13*, 5188-5192.
37. Henkelman, G.; Uberuaga, B. P.; Jónsson, H., A Climbing Image Nudged Elastic Band Method for Finding Saddle Points and Minimum Energy Paths. *J. Chem. Phys.* **2000**, *113*, 9901-9904.
38. Henkelman, G.; Jónsson, H., A Dimer Method for Finding Saddle Points on High Dimensional

Potential Surfaces Using Only First Derivatives. *J. Chem. Phys.* **1999**, *111*, 7010-7022.
39. Arblaster, J. W., Crystallographic Properties of Platinum. *Platinum Met. Rev.* **2006**, *50*, 118-119.
40. Zhou, L.; Kandratsenka, A.; Campbell, C. T.; Wodtke, A. M.; Guo, H., Origin of Thermal and Hyperthermal CO_2 from CO Oxidation on Pt Surfaces: The Role of Post-Transition-State Dynamics, Active Sites, and Chemisorbed CO_2. *Angew. Chem. Int. Ed.* **2019**, *58*, 6916-6920.
41. Silbaugh, T. L.; Karp, E. M.; Campbell, C. T., Energetics of Methanol and Formic Acid Oxidation on Pt(111): Mechanistic Insights from Adsorption Calorimetry. *Surf. Sci.* **2016**, *650*, 140-143.
42. Stamatakis, M.; Chen, Y.; Vlachos, D. G., First-Principles-Based Kinetic Monte Carlo Simulation of the Structure Sensitivity of the Water-Gas Shift Reaction on Platinum Surfaces. *J. Phys. Chem. C* **2011**, *115*, 24750-24762.
43. Guo, H.; Jiang, B., The Sudden Vector Projection Model for Reactivity: Mode Specificity and Bond Selectivity Made Simple. *Acc. Chem. Res.* **2014**, *47*, 3679-3685.
44. Jiang, B.; Guo, H., Relative Efficacy of Vibrational Vs. Translational Excitation in Promoting Atom-Diatom Reactivity: Rigorous Examination of Polanyi's Rules and Proposition of Sudden Vector Projection (SVP) Model. *J. Chem. Phys.* **2013**, *138*, 234104.
45. Uetsuka, H.; Watanabe, K.; Kunimori, K., The Dynamics of Surface Chemical Reactions: Infrared Chemiluminescence of the Product CO_2 Desorbed from Metal Surfaces. *Surf. Sci.* **1996**, *363*, 73-78.
46. Grabow, L. C.; Gokhale, A. A.; Evans, S. T.; Dumesic, J. A.; Mavrikakis, M., Mechanism of the Water Gas Shift Reaction on Pt: First Principles, Experiments, and Microkinetic Modeling. *J. Phys. Chem. C* **2008**, *112*, 4608-4617.
47. Freund, H. J.; Roberts, M. W., Surface Chemistry of Carbon Dioxide. *Surf. Sci. Rep.* **1996**, *25*, 225-273.
48. Behler, J., First Principles Neural Network Potentials for Reactive Simulations of Large Molecular and Condensed Systems. *Angew. Chem. Int. Ed.* **2017**, *56*, 12828-12840.
49. Jiang, B.; Li, J.; Guo, H., High-Fidelity Potential Energy Surfaces for Gas Phase and Gas-Surface Scattering Processes from Machine Learning. *J. Phys. Chem. Lett.* **2020**, *11*, 5120-5131.
50. del Cueto, M.; Zhou, X.; Zhou, L.; Zhang, Y.; Jiang, B.; Guo, H., New Perspectives on CO_2–Pt(111) Interaction with a High-Dimensional Neural Network Potential Energy Surface. *J. Phys. Chem. C* **2020**, *124*, 5174-5181.

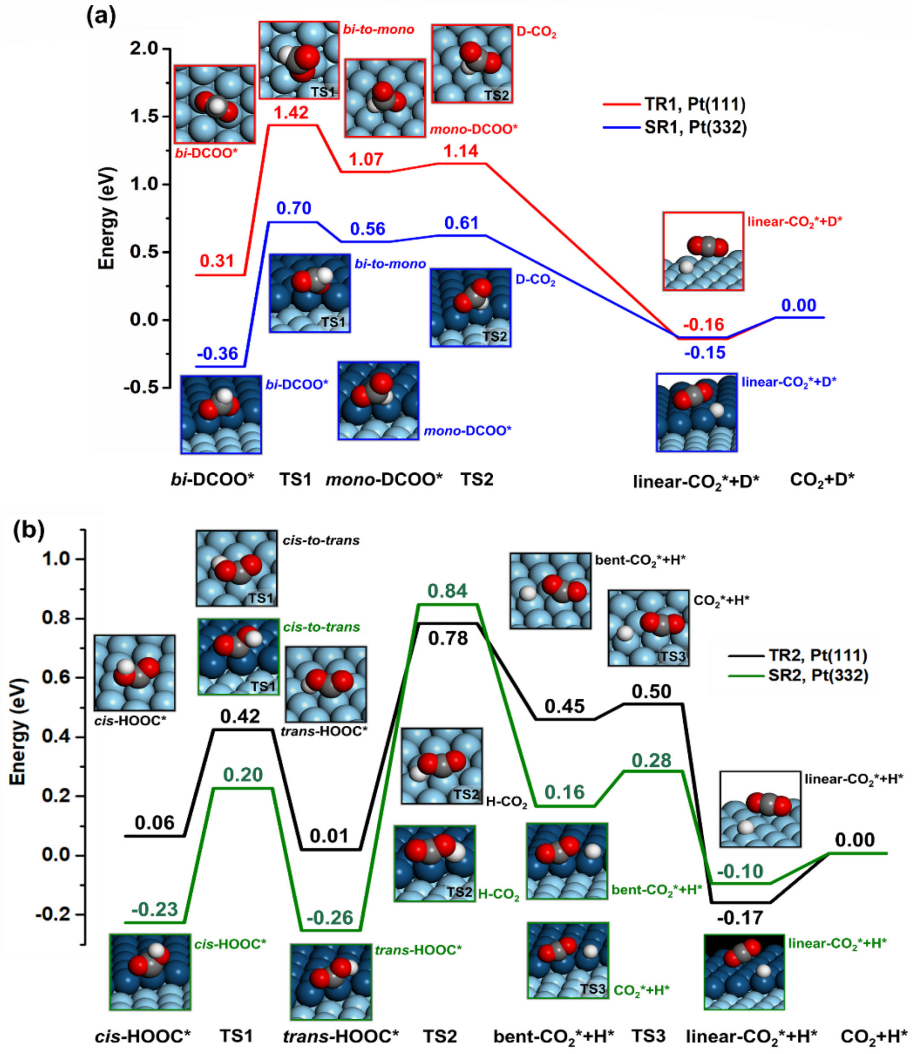

Figure 1. Potential energy diagram of (a) the DCOO* pathway and (b) the HOOC* pathway on the Pt(111) and Pt(332) surfaces. The DCOO* pathway leading to CO_2 + D* on the terrace and step sites are denoted as the TR1 and SR1, respectively with red and blue lines. The HOOC* pathway leading to CO_2 + H* on the terrace and step sites are denoted as the TR2 and SR2, respectively with black and green lines. The energy zero is the sum of the total energies of gas-phase CO_2 and an adsorbed D*/H* on the two surfaces. Structures of the stationary points are shown in the insets. Color codes for structures presented in the inset: White – H, Red – O, Dark Gray – C, Dark Blue/light Blue – Pt.

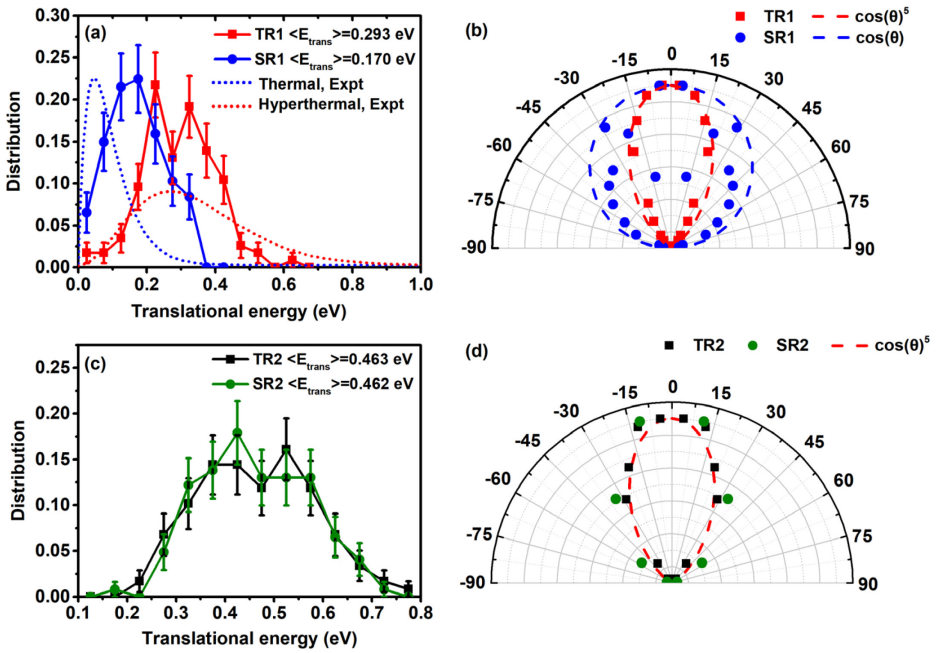

Figure 2. Translational energy distributions of CO_2 that formed by (a) the DCOO* pathway at the terrace site (square, red) and step site (circle, blue), and (b) the HOOC* pathway at the terrace site (square, black) and step site (circle, green). The experimental hyperthermal component (red) and thermal component (blue) distributions[28] are given in dotted lines in (a), respectively. The angular distributions of CO_2 formed by (b) the DCOO* pathway at the terrace site (square, red) and step site (circle, blue), and the (d) the HOOC* pathway at the terrace site (square, black) and step site (circle, green). The $\cos^5(\theta)$ function (red line) or $\cos(\theta)$ function (blue line) in (b) and (d) is the experimental fit to guide eyes. The definitions of TR1, SR1, TR2 and SR2 are the same as Figure 1.

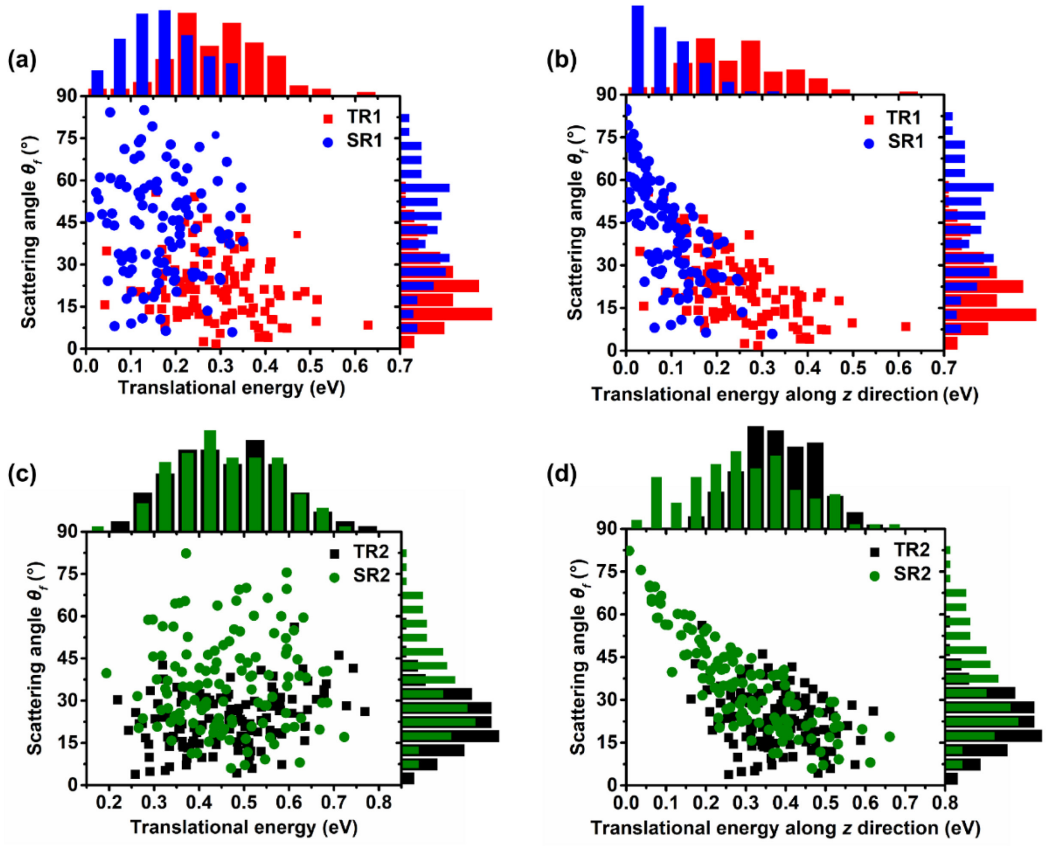

Figure 3. Calculated angular and translational energy distributions of desorbed CO_2 product formed by (a) the DCOO* pathway at the terrace site (red) and step site (blue), and (c) the HOOC* pathway at the terrace site (black) and step site (green). (b, d) same as (a, c), but with translational energies along the surface normal (z). The scattering angle θ_f is defined as the polar angle to the surface normal. The definitions of TR1, SR1, TR2 and SR2 are the same as Figure 1.

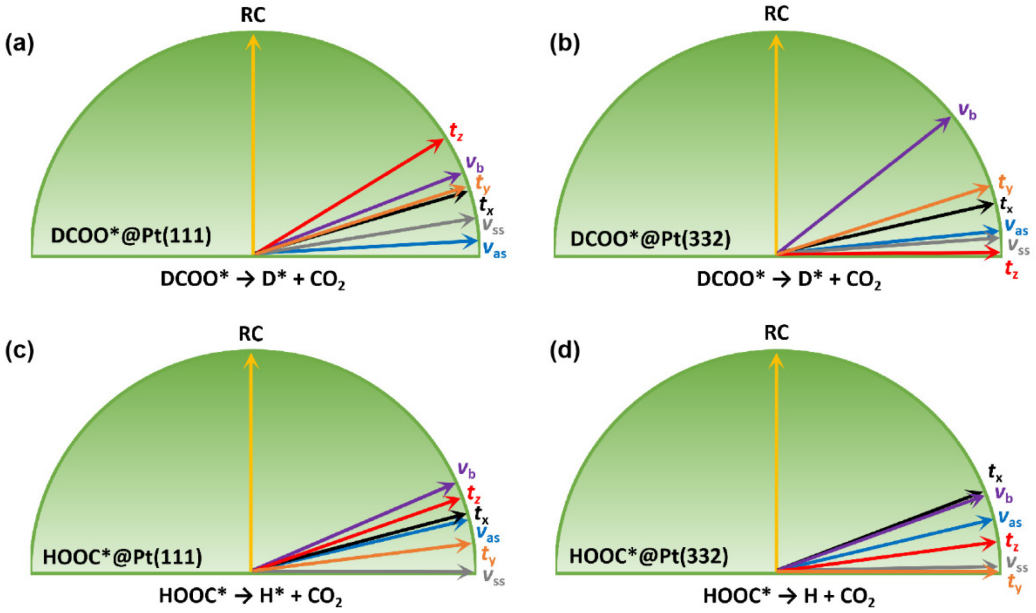

Figure 4. SVP values of the CO_2 translational and vibrational modes onto the reaction coordinate (RC) at TS2 for (a, b) the DCOO* pathway (c, d) HOOC* pathway on the terrace and step sites of Pt(111) and Pt(332), respectively.

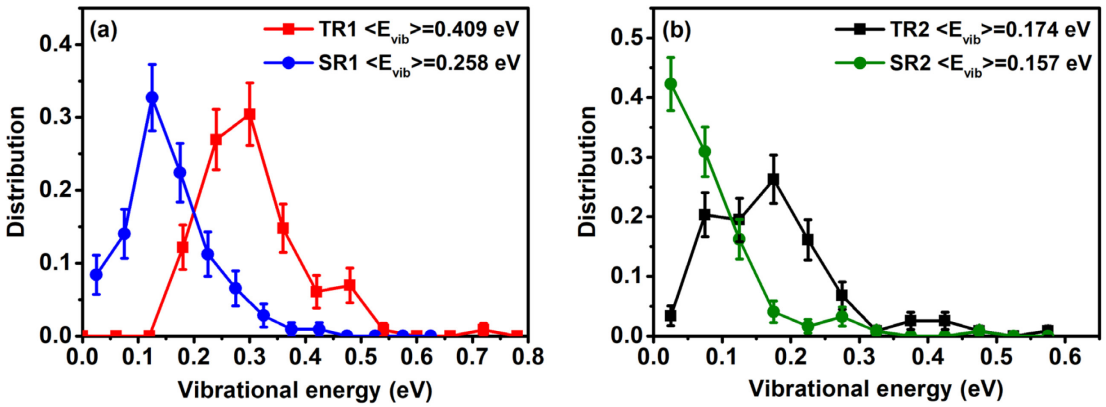

Figure 5. Vibrational energy distributions of CO_2 that formed by (a) the DCOO* pathway at the terrace site (square, red) and step site (circle, blue), and (b) the HOOC* pathway at the terrace site (square, black) and step site (circle, green). The definitions of TR1, SR1, TR2 and SR2 are the same as Figure 1.

TOC graphic

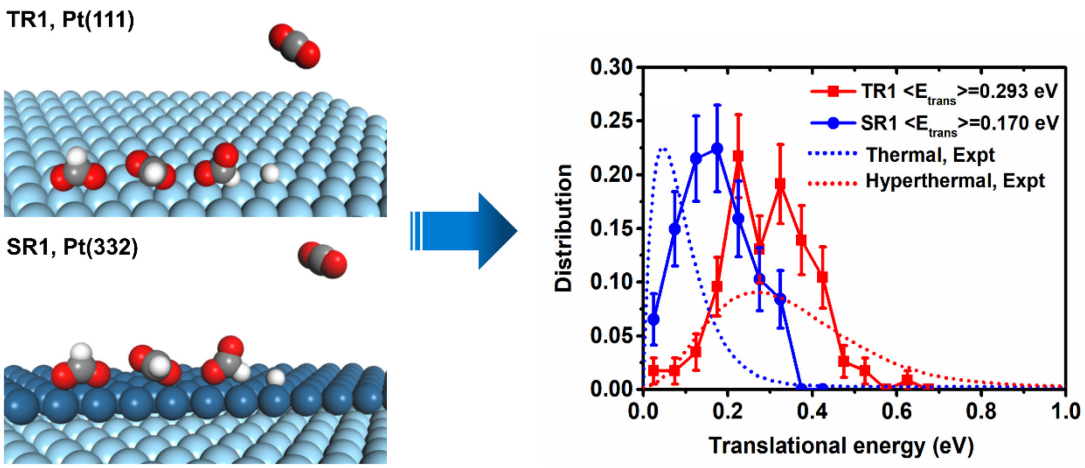
TR1, Pt(111)
SR1, Pt(332)
Distribution
Translational energy (eV)
TR1 <E_trans>=0.293 eV
SR1 <E_trans>=0.170 eV
Thermal, Expt
Hyperthermal, Expt
0.00
0.05
0.10
0.15
0.20
0.25
0.30
0.0
0.2
0.4
0.6
0.8
1.0